12
Fermions on Atom Chips

Marcius H.T. Extavour, Lindsay J. LeBlanc, Jason McKeever, Alma B. Bardon, Seth Aubin, Stefan Myrskog, Thorsten Schumm, and Joseph H. Thywissen

12.1
Introduction

Degenerate Fermi gases (DFGs) earned their place at the leading edge of degenerate quantum gas research with the first demonstration of an atomic ^{40}K DFG in 1999 [1]. Since then, DFGs have been central to many important advances in the field, including molecular Bose–Einstein condensates (BECs), resonant superfluidity, fermion lattice physics, Mott insulator phase, and boson-fermion mixtures (see [2] and references therein).

Not long after the first DFG was produced, efficient loading of cold atoms into atom chip microtraps enabled the first demonstrations of Bose–Einstein condensation on an atom chip [3, 4]. In subsequent years, research efforts in DFGs and atom chips progressed independently, but were combined with the 2006 demonstration in Toronto of a DFG of ^{40}K on an atom chip [5].

In this chapter we provide the background to our work, including ideal fermion statistics and the challenges particular to evaporative cooling in a chip trap. We then describe our observations of Fermi degeneracy in ^{40}K, and of the Ramsauer–Townsend effect. Finally, we discuss several works in progress: species selective manipulation, interaction tuning.

This chapter begins with a review of statistical and thermodynamic properties of the ideal, non-interacting Fermi gas. We discuss our experimental approach to producing a ^{40}K DFG and a ^{40}K-^{87}Rb DFG-BEC mixture, and our observation of the Ramsauer–Townsend effect. We also include a discussion of how trap depth constrains the possible wire geometries for chip traps. Finally, we discuss several works in progress: species selective manipulation, and interaction tuning using a Feshbach resonance.

Atom chips offer a wide array of techniques for trapping and manipulating ultra-cold atoms using a single micro-fabricated device (see Chapter 3). These techniques, discussed extensively in this book, include magnetostatic potentials (see Chapters 1 and 2), electrostatic potentials (see Chapter 13), dynamic radio-

Atom Chips. Edited by Jakob Reichel and Vladan Vuletić

ISBN: 978-3-527-40755-2

frequency (RF) and microwave dressed potentials (see Chapters 7 and 9), and integrated optical potentials (discussed here and in Chapter 3).

With these tools atom chips are well poised to advance active research in fermionic many-body systems. The "Z" trap configuration often used for chip traps makes an elongated potential that, when smooth enough, can produce one-dimensional gases. One-dimensional fermion physics might include Luttinger liquids [6–8], confinement-induced molecule formation [9], and spin-charge separation [10].

RF-dressed double-well potentials on atom chips [11–14] have only recently been applied to ultra-cold fermions [15]. This combination is an exciting step in the direction of fermion quantum atom optics, including interferometry [16], mesoscopic quantum pumping circuit simulations [17], antibunching [18], and number statistics [19–21]. (See also Chapter 7.)

Spin-independent optical potentials can trap the spin mixtures necessary for strong inter-particle interactions in fermions. Optical traps near the surface of an atom chip [22, 23] provide opportunities to combine strongly interacting DFGs with near-field RF and microwave probes. We discuss a first step in this direction in Section 12.7.

Finally, there are several attractive technical advantages in using atom chips for fermions. Large collision rates, made possible by the strong confinement of microtraps relative to conventional, centimeter-scale traps, permit rapid sympathetic evaporative cooling to quantum degeneracy. This obviates the need for minute-scale vacuum lifetimes, multi-chamber vacuum systems, and Zeeman slowers. Dramatically shorter experimental cycle times from atomic vapor to DFG also become possible, a point of practical value in day-to-day laboratory research.

12.2 Theory of Ideal Fermi Gases

Ultra-cold Fermi gases differ from ultra-cold Bose gases in their simplest theoretical description in two important ways: first, there is no macroscopic occupation of the single-particle ground state; second, spin-polarized Fermi gases are completely noninteracting at ultra-cold temperatures [24, 25]. Ideal thermodynamic functions are thus excellent descriptors of cold spin-polarized fermions, even as $T \to 0$. In this section we review fermion thermodynamics, calculate trapped density distributions, and discuss observable signatures of Fermi degeneracy.

12.2.1 Thermodynamics

In the grand canonical ensemble description of an ideal Fermi gas, the mean occupation number of the single-particle energy state ϵ is

$$\langle n_\epsilon \rangle = \frac{1}{e^{\beta(\epsilon-\mu)}+1} = \frac{1}{\mathcal{Z}^{-1}e^{\beta\epsilon}+1}\,, \tag{12.1}$$

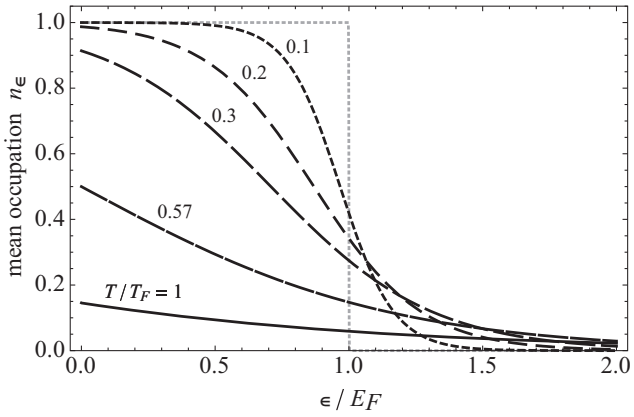

Figure 12.1 Universal curves of the mean Fermi–Dirac occupation of single particle states ϵ vs. ϵ/E_F, shown at select values of T/T_F. The gray, dotted line indicates the $T = 0$ filled Fermi sea (see text).

where $\beta \equiv 1/k_B T$, k_B is the Boltzmann constant, μ is the chemical potential of the gas, and $\mathcal{Z} \equiv e^{\beta\mu}$ is the fugacity. The occupation number is bounded $0 \leq n_\epsilon \leq 1$ as a result of the Pauli exclusion principle. Figure 12.1 shows the occupation number as a function of single-particle energy for various temperatures. The $T = 0$ ideal Fermi gas is characterized by a filled "Fermi sea": all energy levels ϵ for which $\epsilon \leq E_F$ are fully occupied ($n_\epsilon = 1$), while those for which $\epsilon > E_F$ are empty ($n_\epsilon = 0$). The Fermi energy E_F is equal to the chemical potential μ at $T = 0$. At high temperatures the gas is described by a Boltzmann-like distribution [26].

Since a trapped gas is not in contact with number or energy reservoirs in experiments, we ignore fluctuations in the total number and energy predicted by the grand canonical ensemble description, taking N and E to be the *average* total number and total energy, respectively. These can be calculated using the discrete sums

$$N = \sum_\epsilon \langle n_\epsilon \rangle \quad \text{and} \quad E = \sum_\epsilon \epsilon \langle n_\epsilon \rangle \,, \tag{12.2}$$

where the sums run over all discrete states. In the limit of a large number of occupied states we can take the continuum limit, writing

$$N = \int_{\epsilon=0}^{\infty} g(\epsilon)\langle n_\epsilon \rangle \mathrm{d}\epsilon \quad \text{and} \quad E = \int_{\epsilon=0}^{\infty} g(\epsilon)\epsilon\langle n_\epsilon \rangle \mathrm{d}\epsilon \,, \tag{12.3}$$

where $g(\epsilon) = \epsilon^2/2(\hbar\bar{\omega})^3$ is the energy density of states for a harmonically trapped gas in three dimensions, and $\bar{\omega} \equiv (\omega_x \omega_y \omega_z)^{1/3}$ is the geometric mean harmonic trap frequency.

Integrals of this type can be evaluated using the Fermi–Dirac integrals [26]

$$f_n(C) \equiv \frac{1}{\Gamma(C)} \int_0^\infty \frac{a^{n-1} da}{C^{-1}e^a + 1} = -\mathrm{Li}_n(-C) \quad (0 \leq C < \infty \,,\ n > 0) \,, \tag{12.4}$$

where $\mathrm{Li}_n(C) = \sum_{j=1}^{\infty} C^j/j^n$ is a polylogarithmic function and $\Gamma(C)$ is the gamma function. For $n = 1$, $f_1 = \ln(1 + C)$. Using Eq. (12.4) we find that the average total number and energy are

$$N = (\beta\hbar\bar{\omega})^{-3} f_3(\mathcal{Z}) \quad \text{and} \quad E = 3k_B T(\beta\hbar\bar{\omega})^{-3} f_4(\mathcal{Z}) \,. \tag{12.5}$$

The number and energy at zero temperature can be found using the zero temperature limit of the Fermi function,

$$\lim_{T\to 0} f_n(\mathcal{Z}) = \frac{(\beta\mu)^n}{\Gamma(n+1)} \,. \tag{12.6}$$

As mentioned above, the Fermi energy E_F is defined as the zero temperature limit of μ. For convenience, we will also refer to the "Fermi temperature" $T_F \equiv E_F/k_B$, even though this temperature does not correspond to a phase transition, as is the case for T_c of Bose gases. Re-writing Eq. (12.5) in terms of E_F, we find

$$N = \frac{1}{6}\left(\frac{E_F}{\hbar\bar{\omega}}\right)^3 \quad \text{and} \quad E = \frac{3}{4} N E_F \,. \tag{12.7}$$

The chemical potential and fugacity at finite temperature can be found numerically by solving

$$6 f_3(\mathcal{Z}) = (\beta E_F)^3 \,. \tag{12.8}$$

Using the Sommerfeld expansion of the polylogarithms, one obtains low- and high-temperature approximations to the chemical potential in a three-dimensional harmonic trap [28]:

$$\mu \approx \begin{cases} E_F\left[1 - \frac{\pi^2}{3}\left(\frac{k_B T}{E_F}\right)^2\right] & \text{for } k_B T \ll E_F \,, \quad \text{and} \\ -k_B T \ln\left[6\left(\frac{k_B T}{E_F}\right)^3\right] & \text{for } k_B T \gg E_F. \end{cases} \tag{12.9}$$

Low Dimensionality Under certain conditions, a $T = 0$ Fermi gas in an anisotropic magnetic trap having $\omega_\perp \gg \omega_\parallel$ may become effectively one dimensional. If the atom number and temperature are such that $E_F < \hbar\omega_\perp$, the transverse degrees of freedom are "frozen out" and fermions occupy only the longitudinal energy levels of the trap. The maximum number of fermions N_{1D} that can populate such a one-dimensional configuration at $T = 0$ is equal to the aspect ratio of the trap: $N_{1D} = \omega_\perp/\omega_\parallel$. This scenario is especially relevant to atom chip micro-magnetic traps, whose aspect ratios can be on the order of 10^2 to 10^4 [29].

12.2.2 Density Distribution

Apart from the choice of $g(\epsilon)$, many of the expressions derived in Section 12.2.1 resemble the textbook treatment of a uniform Fermi gas. In this section, we calculate

the non-uniform position and momentum distributions of *trapped* fermions. The position distribution is observable *in situ* (with sufficient spatial resolution), while the momentum distribution is observable in time-of-flight. We calculate these distributions by two different conceptual starting points: first, using semi-classical integrals; and second, using the local density approximation.

Semi-Classical Approximation Taking the energies $\epsilon \equiv \epsilon(\boldsymbol{r}, \boldsymbol{p}) = p^2/2M + U(\boldsymbol{r})$ to be those of a classical free particle at position $\boldsymbol{r}$, where $U(\boldsymbol{r})$ is the trapping potential and M is the atomic mass, we can integrate the occupation function of Eq. (12.1) over the momentum degrees of freedom to find the semi-classical position distribution:

$$n(\boldsymbol{r}) = \int \frac{d^3p}{(2\pi\hbar)^3} \left[\mathcal{Z}^{-1} \mathrm{e}^{\beta\epsilon(\boldsymbol{r},\boldsymbol{p})} + 1\right]^{-1} , \tag{12.10}$$

in which we have used the semi-classical phase-space volume of one quantum state, $(2\pi\hbar)^3$. Integration using Eq. (12.4) yields

$$n(\boldsymbol{r}) = \Lambda_T^{-3} f_{3/2}\left(\mathcal{Z}\mathrm{e}^{-\beta U(\boldsymbol{r})}\right) , \tag{12.11}$$

where $\Lambda_T = \sqrt{2\pi\hbar^2\beta/M}$ is the thermal de Broglie wavelength. Unlike the corresponding expression for ideal bosons, Eq. (12.11) is valid *at all temperatures*. The difference lies in the fact that we have ignored the occupation of the single-particle ground state in taking the continuum limit (see Eq. (12.3)), evidenced by the vanishing density of states $g(\epsilon)$ for $\epsilon = 0$. This does not pose a problem for fermions, for which the occupation of the ground state $\mathcal{Z}/(1+\mathcal{Z}) \leq 1$. For bosons, however, the corresponding expression $\mathcal{Z}/(1-\mathcal{Z})$ diverges; the continuum limit completely ignores the condensed fraction, whose contribution to the thermodynamics must be accounted for separately [26].

Local Density Approximation An alternate conceptual approach to the calculation of inhomogeneous distributions is the local density approximation. We start with the expression for the density of a *uniform* Fermi gas $n_{\mathrm{uniform}} = \Lambda_T^{-3} f_{3/2}(\mathcal{Z})$ [26] and assume that local properties can be described by a local chemical potential $\mu - U(\boldsymbol{r})$ and hence a local fugacity $\mathcal{Z}\mathrm{e}^{-\beta U(\boldsymbol{r})}$. We immediately recover Eq. (12.11), and obtain its zero-temperature using Eq. (12.6)

$$n_{\mathrm{uniform}} \xrightarrow{T=0} \frac{1}{6\pi^2}\left[\frac{2M}{\hbar^2} E_{\mathrm{F}}\right]^{3/2} . \tag{12.12}$$

This implies that long-range properties of the Fermi gas may be ignored, unlike in a BEC, which exhibits long-range phase coherence. In fact, the local density approximation and the semi-classical approach generally yield identical results for non-interacting fermions [24].

Specializing to the case of a three-dimensional harmonic oscillator potential $U(\boldsymbol{r}) = \frac{1}{2}M(\omega_x^2 x^2 + \omega_y^2 y^2 + \omega_z^2 z^2)$ we obtain

$$n(\boldsymbol{r}) = \Lambda_T^{-3} f_{3/2}\left(\mathcal{Z}\exp\left[-\frac{\beta M}{2}\left(\omega_x^2 x^2 + \omega_y^2 y^2 + \omega_z^2 z^2\right)\right]\right) . \tag{12.13}$$

At zero temperature,

$$n(\boldsymbol{r}) = \frac{8N}{\pi^2 \bar{R}_{\mathrm{TF}}^3}\left[1 - \frac{x^2}{X_{\mathrm{TF}}^2} - \frac{y^2}{Y_{\mathrm{TF}}^2} - \frac{z^2}{Z_{\mathrm{TF}}^2}\right]^{3/2} \Theta\left(1 - \frac{x^2}{X_{\mathrm{TF}}^2} - \frac{y^2}{Y_{\mathrm{TF}}^2} - \frac{z^2}{Z_{\mathrm{TF}}^2}\right) \tag{12.14}$$

where $\bar{R}_{\mathrm{TF}} = \sqrt{2E_{\mathrm{F}}/M\bar{\omega}^2}$ is the mean Thomas–Fermi radius of the cloud, $X_{\mathrm{TF}} = \sqrt{2E_{\mathrm{F}}/M\omega_x^2}$ and so on are the Thomas–Fermi lengths along each trapping axis, and $\Theta(\cdots)$ is the Heaviside step function.

The momentum distribution can also be calculated using either the local density or semi-classical approach. Experimentally, we observe the momentum distribution in a time-of-flight density image, for which the distribution is obtained by rescaling all spatial coordinates

$$\frac{x_i \to x_i}{\sqrt{1 + \omega_i^2 t^2}}$$

in Eq. (12.13) along the direction $i \in \{x, y, z\}$, and renormalizing to conserve particle number [25].

12.2.3 Crossover to Fermi Degeneracy

The $T = 0$ filled Fermi sea is quantum degenerate in the sense that it represents the absolute many-particle ground state of this non-interacting system. The meaning of the term "degenerate" here should not be confused with its more conventional meaning for a gas of bosons, for which degeneracy implies multiple or macroscopic occupation of the single-particle ground state (see Chapter 2). Multiple occupancy is forbidden for fermions, and so they are always "nondegenerate" in the more conventional sense of the word.

What, then, is the nature of the transition to quantum degeneracy in fermions? In contrast to the boson case, there is no phase transition into or out of the filled Fermi sea. As is the case with bosons, however, high-temperature expansions for thermodynamic quantities fail around $\mathcal{Z} = 1$. At lower temperatures the behavior differs dramatically from the predictions of classical, Boltzmann statistics. As $T \to 0$, $\mathcal{Z} \to 1^-$ for ideal bosons, whereas $\mathcal{Z} \to \infty$ for ideal fermions with the scaling $\mathcal{Z} \approx \mathrm{e}^{\beta E_{\mathrm{F}}}$, as implied by Eq. (12.9). It is interesting to note the quantitative relationship between fugacity and degeneracy for fermions:

$$n_0 \Lambda_T^3 = f_{3/2}(\mathcal{Z}) \,, \tag{12.15}$$

where $n_0 \equiv n(0)$ is the central density of the cloud. Thus, $n_0\Lambda_T^3 \simeq 0.77$ when $\mathcal{Z} = 1$ for fermions, which occurs at $T \simeq 0.57T_{\mathrm{F}}$. By comparison, $n_0\Lambda_T^3 \simeq 2.61$ when $\mathcal{Z} = 1$ for bosons, at $T = T_{\mathrm{c}}$.

The lack of a marked phase transition raises the question of what an experimental signature of Fermi degeneracy might be. Unlike a BEC, the non-interacting

DFG has an isotropic momentum distribution in time-of-flight, even when released from an anisotropic trap [28]. Thus, the aspect ratio of the cold cloud cannot be a signature of degeneracy. Instead, observations of Fermi degeneracy rely on two signatures: the average energy per particle, and the shape of the time-of-flight density distribution.

Using Eq. (12.5) we may write the average energy per particle as

$$\frac{E}{N} = 3k_{\mathrm{B}}T\frac{f_4(\mathcal{Z})}{f_3(\mathcal{Z})}\,. \tag{12.16}$$

The finite zero-temperature limit of Eq. (12.16) is $3E_{\mathrm{F}}/4$, corresponding to Fermi pressure [26, 27]. By comparison, the corresponding expression for the Boltzmann gas is $E/N = 3k_{\mathrm{B}}T$, which tends toward zero at zero temperature.

The second signature of Fermi degeneracy is evident when the observed fermion time-of-flight distribution is compared to the predictions of the Boltzmann and Fermi–Dirac models. The latter is obtained by integration of Eq. (12.13) along the imaging line of sight.[28)]

Taking z as the imaging direction, we find

$$\tilde{n}(x,y,t) = \frac{N}{2\pi r_x(t) r_y(t) f_3(\mathcal{Z})} f_2\left(\mathcal{Z}\exp\left[-\frac{x^2}{2r_x^2(t)} - \frac{y^2}{2r_y^2(t)}\right]\right), \tag{12.17}$$

where $r_i^2(t) = (\omega_i^{-2} + t^2)/\beta M$ is the cloud size in the $i \in \{x, y, z\}$ direction after a time t of free expansion. By comparison, the spatial distribution for an expanding cloud of classical particles is

$$\tilde{n}_{\mathrm{cl}}(x,y,t) = \frac{N}{2\pi r_x(t) r_y(t)} \exp\left[-\frac{x^2}{2r_x^2(t)} - \frac{y^2}{2r_y^2(t)}\right], \tag{12.18}$$

using the same definitions for $r_i(t)$. Both of these signatures have been observed, as discussed further in Section 12.5.5.

12.3 The Atom Chip

The experiments described in this chapter were carried out at the University of Toronto with an atom chip designed and fabricated in the atom chip group at the Laboratoire Charles Fabry de l'Institut d'Optique [30, 31]. This section details the conductor layout, material composition, and supporting electrical and mechanical infrastructure for the chip. See Chapter 3 for a more thorough review of atom chip fabrication.

28) When integrating Fermi functions over Gaussian degrees of freedom, it is useful to note that $\int_{-\infty}^{\infty} \mathrm{d}x\, f_n(C\mathrm{e}^{-x^2}) = \sqrt{\pi} f_{n+1/2}(C)$.

12.3.1
Chip Construction and Wire Pattern

The atom chip consists of gold wires electroplated onto a cleaved 16 mm × 28 mm × 600 μm silicon substrate. The chip was patterned using photolithography, with the metal wires deposited by evaporation and electroplating. A 20-nm titanium adhesion layer and 200-nm gold seed layer were evaporated onto the SiO_2 surface oxide, followed by solution electroplating of gold to a final wire height of 6 μm. The final result is a mostly bare silicon substrate hosting eight gold electrical contact pads connecting five separate conductors on its surface [30]. The wires can sustain an operating DC current of 5 A, though we never exceed 2 A in the central Z-wire.

We use two of the five chip wires in the work presented here, highlighted in dark gray in Figure 12.2a. The central Z-wire forms the basis of our static micromagnetic trap. An adjacent, thinner wire is used as a near-field antenna for delivering RF and microwave fields to the trapped atoms.

12.3.2
Electrical and Mechanical Connections

The chip is fastened to a copper support "stack" without glue or screws, but by mechanical pressure only. Custom-made MACOR ceramic C-clamps press flattened strips of beryllium-copper foil onto the gold contact pads for DC and RF electrical connections, while at the same time pressing the chip onto the stack (see

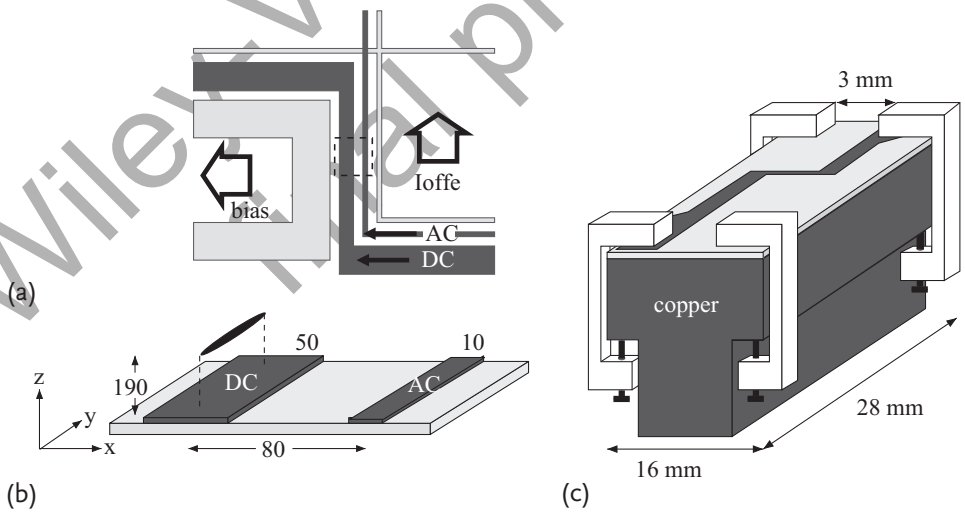

Figure 12.2 Atom chip conductor pattern and mounting schematic diagram. (a) Central atom chip conductor pattern, highlighting the Z-wire ("DC") and adjacent, thinner antenna wire ("AC") in dark gray. Thick arrows indicate the directions of external, uniform magnetic fields. (b) Close-up view of dashed region in (a), showing wire widths, center-to-center separation, and location of the trapped atomic cloud (black ellipsoid). All dimensions are in micrometers. (c) The atom chip is pressed onto a fly-cut copper block using ceramic MACOR C-clamps (white). Electrical connections are not shown.

Figure 12.2c). The beryllium-copper foil strips are in turn connected to ceramic-insulated copper wires which deliver current from the air side into the UHV chamber and onto the chip. The entire assembly is mounted vertically in the vacuum chamber with the atom chip at the bottom, face down [32, 33]. The stack also acts as a heat-sink for the atom chip, and was machined from oxygen-free high-conductivity (OFHC) copper.

12.3.3 The Z-Wire Magnetic Trap

We use an anisotropic, Ioffe–Pritchard-type Z-wire microtrap [34] throughout (see also Chapters 1 and 2). The external DC bias fields used for magnetic confinement are supplied by three pairs of magnetic field coils mounted outside of the vacuum chamber. With this setup we have achieved atom–surface distances between 80 μm and 300 μm, harmonic oscillation frequencies $\omega_{x,z} \sim 2\pi \times 200$ Hz to $2\pi \times 2.5$ kHz, $\omega_y \sim 2\pi \times 32$ to 50 Hz, and trap depths as large as $k_B \times 1.4$ mK.

The effects of wire surface roughness on the magnetic potential have been studied extensively for atom chips of this type [30, 35, 36]. Though sub-micrometer-scale wire rugosity is not a problem at our 190-μm working distance, we do observe three large and unexpected minima in the longitudinal magnetic potential. Though these "defects" prevent us from reaching the largest trap anisotropies available in Z-traps, we use them to our advantage during evaporative cooling. Magnetic gradients applied along y tilt the longitudinal potential so that atoms preferentially fill the largest and deepest of these local potential minima. In this local trap, the longitudinal oscillation frequency is two to three times larger than it would be in the absence of the defect. The increased mean oscillation frequency $\bar{\omega}$ (see Section 12.2.1) and accompanying gains in collision rate allow us to evaporate to quantum degeneracy more rapidly and efficiently than would otherwise be possible.

12.4 Loading the Microtrap

Our experimental approach to creating a ^{40}K DFG on an atom chip is motivated in large part by the scarcity of ^{40}K, whose natural isotopic abundance is only 0.012 %. Even when using a potassium dispenser with ^{40}K enriched to 5 %, we find that large MOT beams are essential to capture enough ^{40}K in a background UHV pressure compatible with magnetic trapping. Rather than using a reflected surface MOT [37], which would require a mirror-coated chip of length $\sim$ 6 cm to accommodate our 4-cm-diameter MOT beams, we first load a large conventional MOT several centimeters beneath the atom chip, then magnetically trap and transport the atoms to the chip. Once loaded into the Z-trap, we sympathetically cool ^{40}K to quantum degeneracy with a ^{87}Rb reservoir to minimize ^{40}K atom number loss. This approach also obviates the need for a mirror-coated atom chip.

In this section and the next, we review our laser cooling, magnetic trapping and transport, chip loading, and evaporative cooling steps, noting that further detail is available in [5, 15, 32]. We also add to our previous work with a discussion of the roles of trap depth and trap volume in micro-trap experiments, with particular emphasis on chip loading in our setup.

12.4.1 Laser Cooling and Magnetic Transport to the Chip

Both ^{40}K and ^{87}Rb are initially trapped and cooled in a dual-species MOT formed by six counter-propagating 4-cm-diameter beams centered 5 cm below the atom chip [15, 32]. We use a single-chamber vacuum system, and load the MOT directly from atomic vapor created using a combination of dispensers and light-induced atom desorption (LIAD). During each MOT loading cycle, commercial high-power 405-nm LEDs irradiate our 75 mm × 75 mm × 160 mm Pyrex vacuum cell for several seconds to generate the atomic vapor. We use commercial Rb and home-made K dispensers to replenish the ^{40}K and ^{87}Rb coatings on the interior walls of the UHV chamber as needed – typically every few days or weeks [15]. By this method we achieve ^{40}K and ^{87}Rb atom numbers of roughly 6×10^6 and 6×10^8 in the MOT.

After optical molasses cooling of ^{87}Rb, both ^{87}Rb and ^{40}K are optically pumped into the stretched internal magnetic hyperfine states, $|F = 2, m_F = 2\rangle$ and $|F = 9/2, m_F = 9/2\rangle$, respectively. With all lasers extinguished, the mixture is magnetically trapped in a quadrupole magnetic trap and transported vertically to the surface of the atom chip using external coils. From there atoms are smoothly transferred from the quadrupole magnetic trap into the Z-trap located 190 µm from the chip surface, which has harmonic ^{40}K oscillation frequencies $\omega_{x,z} = 2\pi \times 823 \pm 7$ Hz and $\omega_y = 2\pi \times 46 \pm 1$ Hz, and a trap depth of $\sim k_B \times 1.05$ mK.

12.4.2 Loading Bosons and Fermions onto the Atom Chip

Along with the advantages of high compression and fast collision rate characteristic of atom chip microtraps comes a disadvantage: small trap volume. The volume occupied by a trapped gas depends on its temperature, unlike in the uniform "box" potential we are accustomed to from thermodynamics. The trap volume is not typically discussed when creating "macroscopic" magnetic traps with large coils, since their trap depths can be orders of magnitude larger than is required to confine laser-cooled atoms. For microtraps, however, the trap volume may limit the number of atoms that can "fit" into the trap, in a way that we will quantify in the following subsections. Our discussion points out a clear route to larger atom number, when it would be desirable.

An atom is trapped when its energy is less than the trap depth U_{td}. A good model of a thermalized gas in a trap-depth-limited trap is a truncated Boltzmann distribution [38], where truncation occurs at η times the temperature, that is

$U_{\rm td} = \eta k_{\rm B} T$. For the collision rates typical of atom chip traps, free evaporation resulting from the limited trap depth occurs when $\eta \lesssim 3$; by contrast, *efficient* evaporation occurs when $\eta \gtrsim 5$.

The laser cooling discussed in Section 12.4.1 allows atoms to be delivered to the chip at temperatures less than $U_{\rm td}$. However, our loading efficiency is typically 10 % or less, while phase-space density is roughly preserved: we load roughly 2×10^7 ^{87}Rb atoms and 2×10^5 ^{40}K into the Z-trap. We will attempt to explain the factors limiting this efficiency in the following subsections.

The initial loaded number of fermions places an upper bound on the number of ultra-cold fermions we can produce. Furthermore, though we load many more bosons than fermions, bosons are continually lost during the evaporative cooling process, as described in Section 12.5.1. The limited amount of "refrigerant" eventually limits the number of fermions that can be cooled, or their final temperature. It is, therefore, important to understand our loading process and ways in which it can be improved.

12.4.3
Effective Trap Volume

Our discussion here concerns the number, temperature, and density of a gas at the start of evaporative cooling, having already been loaded into the microtrap. We will assume an initial phase-space density ρ_0, which is typically $\lesssim 10^{-5}$ for laser-cooled atoms. At the densities typical of this point in the experimental cycle, the density distribution of the gas is well approximated as that of an ideal non-degenerate gas.

From Eq. (12.11), the density distribution of an ideal Fermi gas in three dimensions is $n(\boldsymbol{r}) = \Lambda_T^{-3} f_{3/2}(\mathcal{Z} {\rm e}^{-\beta U(\boldsymbol{r})})$, where $U(0) \equiv 0$. The corresponding expression for ideal bosons is obtained by using the thermodynamic Bose–Einstein function $g_{3/2}(\cdots)$ in place of $f_{3/2}(\cdots)$ in this expression. In either case, at low fugacity

$$n(\boldsymbol{r}) \xrightarrow{\mathcal{Z}\ll 1} \Lambda_T^{-3} \mathcal{Z} {\rm e}^{-\beta U(\boldsymbol{r})} \,. \tag{12.19}$$

Integrating both sides of the equation, we recover the total atom number

$$N = n_0 \int {\rm e}^{-\beta U(\boldsymbol{r})} d\boldsymbol{r} \,, \tag{12.20}$$

where the volume of integration is defined by $U < U_{\rm td}$, and $n_0 = n(0)$.

In analogy with a uniform gas, we define the effective volume

$$V_{\rm eff} \equiv \int {\rm e}^{-\beta U(\boldsymbol{r})} d\boldsymbol{r} \,, \tag{12.21}$$

such that $n_0 = N/V_{\rm eff}$ [38]. For a simple three-dimensional box of side L, $V_{\rm eff} = V = L^3$.

In the limit of $\eta \gg 1$, we can integrate the full Boltzmann distribution to find the trap volume in several typical cases. For a three-dimensional simple harmonic

oscillator potential,

$$V_{\text{eff}}^{\text{SHO}} = \left(\frac{2\pi}{M\bar{\omega}^2}\right)^{\frac{3}{2}} (k_{\text{B}}T)^{\frac{3}{2}} , \tag{12.22}$$

where $\bar{\omega}$ is the geometric mean oscillation frequency. For the three-dimensional quadrupole (linear) trap,

$$V_{\text{eff}}^{\text{QT}} = 8\pi \bar{F}^{-3} (k_{\text{B}}T)^3 , \tag{12.23}$$

where $U \equiv |\boldsymbol{F} \cdot \boldsymbol{r}|$ and $\bar{F}$ is the geometric mean gradient. Finally, a hybrid two-dimensional quadrupole and one-dimensional box model gives

$$V_{\text{eff}}^{\text{2QB}} = 2\pi L \bar{F}^{-2} (k_{\text{B}}T)^2 . \tag{12.24}$$

In all of the above cases, the effective volume has a power-law dependence $V_{\text{eff}} = C_\delta T^\delta$.

12.4.4 A Full Tank of Atoms: Maximum Trapped Atom Number

Using the effective volume, we can now relate the trapped atom number to the initial phase-space density ρ_0, which is equivalent to the degeneracy parameter $n_0 \Lambda_T^3$ for $\mathcal{Z} \ll 1$:

$$N = \rho_0 \Lambda_T^{-3} V_{\text{eff}}(T) . \tag{12.25}$$

Since $k_{\text{B}}T = U_{\text{td}}/\eta$ by definition, we can write out the explicit temperature dependence in Eq. (12.25) to find

$$N_{\text{max}} = \rho_0 \left(\frac{M}{2\pi\hbar^2}\right)^{\frac{3}{2}} C_\delta \left(\frac{U_{\text{td}}}{\eta}\right)^{\delta+\frac{3}{2}} , \tag{12.26}$$

for a trap with a δ power law effective volume.

This equation shows us why the loaded atom number is typically smaller in microtraps than macrotraps. First, the trap depth U_{td} is typically smaller, which reduces atom number with a power law as fast as $U_{\text{td}}^{9/2}$ for a three-dimensional quadrupole. Second, even for comparable trap depths, the stronger trapping strength of a microtrap reduces C_δ: $C_3 \propto \bar{\omega}^{-3}$ in the case of a three-dimensional harmonic oscillator, for instance.

Equation (12.26) also demonstrates the importance of large currents in trapping wires. Consider the case in which a three-dimensional harmonic microtrap is formed above a single long wire, for which $\omega_\perp \propto B_{0\perp}/I$ where $B_{0\perp}$ is the perpendicular bias field and I is the wire current. Since the trap depth increases linearly with $B_{0\perp}$, Eq. (12.26) suggests that the maximum atom number at a fixed η and phase-space density is $N_{\text{max}} \propto I^2 B_{0\perp}/\omega_z$. Assuming that the distance from the trapped atoms to the chip surface is fixed, and that $\omega_z \propto \sqrt{I}$, $N_{\text{max}} \propto I^{5/2}$. Thus, we see that larger wire currents allow an increase in the number of trapped atoms.

12.4.5
Effect of Geometry on Loaded Atom Number

We now evaluate the trap volume and the expected maximum atom number loaded into several well-studied chip traps. We will start with the earliest proposed traps, described in [39] by Libbrecht, and assume they are loaded with ^{87}Rb in the $|2,2\rangle$ state. For a single-loop quadrupole trap of radius 10 μm and using a 1-A current, the gradient is 5.4×10^5 G/cm and the trap depth $k_B\times21$ mK. Assuming the trap can be loaded with $\eta \geq 4$ (corresponding to an initial temperature of ≤ 5 mK), the trap volume would be $V_{\text{eff}} \leq 310\ \mu\text{m}^3$. At an initial phase-space density of 10^{-6}, 2×10^4 atoms could be loaded into the trap. However, a quadrupole trap has a magnetic field zero at its center, and is thus unsuitable for trapping ultra-cold atoms.

The Ioffe "(c)" configuration of [39] consists of concentric half-loops with a 10 μ minimum diameter. Using a 1-A current, the trap has a depth of $k_B\times1.3$ mK and a curvature that gives $\bar{\omega}/2\pi \approx 94$ kHz. Although the trap is impressively strong, its effective volume is only 0.4 μm^3; less than one atom would be trapped at a phase-space density of 10^{-6}. For this reason, larger trap volumes than those of Libbrecht's pioneering geometries were required to achieve quantum degeneracy in an atom chip microtrap.

Finally, let us consider the Reichel Z-trap [37] (see also Chapter 2). The potential at the center of the trap is harmonic, with a typical geometric mean frequency of $\bar{\omega}/2\pi \approx 300$ Hz in our setup. The trap depth is limited by the transverse applied field, for which a typical value of 20 G gives $U_{\text{td}} \approx k_B \times 1.3$ mK. Assuming the trap is loaded at $\eta = 4$, we find that the effective volume is $1.3\times10^7\ \mu\text{m}^3$, and the maximum trapped atom number 1.2×10^7 at an initial phase-space density of 10^{-6}. Although approximate, our calculation shows that the Z-trap geometry is capable of loading six to seven orders of magnitude more atoms than the Libbrecht geometry for the same initial phase-space density.

Furthermore, the calculation suggests that the loaded atom number in our experiment is limited by trap depth and volume. For our geometric mean field curvature of 3×10^4 G/cm^2 and initial temperature of 300 μK, the effective trap volume is $3\times10^7\ \mu\text{m}^3$. One would expect 3×10^7 ^{87}Rb atoms at $\rho_0 \approx 10^{-6}$, and 3×10^5 ^{40}K atoms at $\rho_0 \approx 4\times10^{-8}$. This is consistent with our observations to within an order-of-magnitude (2×10^7 for ^{87}Rb and 2×10^5 for ^{40}K), and demonstrates that we are close to, if not at, the maximum possible number of loaded atoms, given the phase-space density and temperature after magnetic transport to the chip.

12.5
Rapid Sympathetic Cooling of a K-Rb Mixture

In this section we describe the sympathetic evaporative cooling of ^{40}K with ^{87}Rb in a microtrap, by which we produce a pure ^{40}K DFG or a dually degenerate BEC–DFG mixture. Particular emphasis is placed on the temperature dependence of the K-Rb scattering length, and its effect on K-Rb rethermalization and evaporation

efficiency. The section concludes with a discussion of experimental signatures of quantum degeneracy in DFGs.

12.5.1
Forced Sympathetic RF Evaporation

We reach dual quantum degeneracy in ^{40}K and ^{87}Rb via sympathetic RF evaporative cooling of ^{87}Rb in a Z-trap having $B_0 \simeq 2.6$ G, ^{40}K harmonic oscillation frequencies $\omega_{x,z} = 2\pi\times 823\pm 7$ Hz and $\omega_y = 2\pi\times 46\pm 1$ Hz, and a trap depth of $k_B\times 1.05$ mK [5, 40–43]. In our case, ^{40}K is cooled indirectly by thermalizing elastic collisions with ^{87}Rb. By sweeping the RF evaporation frequency from 28.6 to 3.65 MHz in as little as 6 s, we reach $T/T_F \simeq 0.1 - 0.2$ with $\epsilon_F \simeq k_B \times 1.1$ μK and as many as 4×10^4 ^{40}K atoms, faster than has been possible in conventional magnetic traps [5, 15].[29] This rapid evaporation to degeneracy is made possible by the strong atom chip confinement.

As is evident in Figure 12.3, the ^{40}K is cooled to quantum degeneracy ($\mathcal{Z} \geq 1$) with only a five-fold loss in atom number, while the ^{87}Rb is evaporated with log-slope efficiency $-\partial[\log(\rho_0)]/\partial[\log(N)] = 2.9 \pm 0.4$, where ρ_0 is the peak phase-space density. When evaporating ^{87}Rb alone to BEC, the evaporation efficiency can be as high as 4.0 ± 0.1; sacrificing some evaporation efficiency, a more rapid evaporation can produce a BEC in just 2 s. By contrast, for ^{40}K-^{87}Rb mixtures, we observe that RF sweep times faster than 6 s are not successful in achieving dual degeneracy. The reason is that ^{87}Rb and ^{40}K rethermalize more slowly than ^{87}Rb alone, particularly

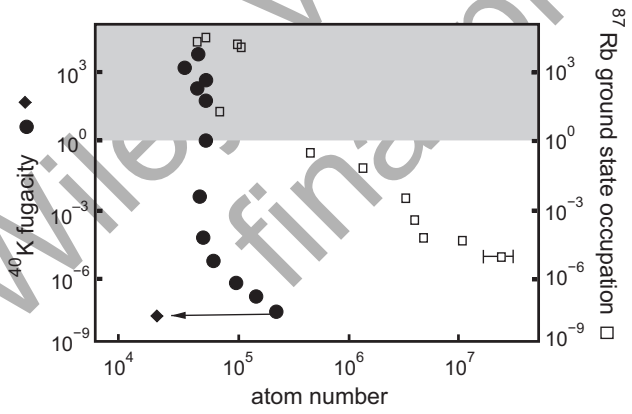

Figure 12.3 Sympathetic cooling to dual ^{40}K-^{87}Rb quantum degeneracy. Spin-polarized fermions without a bosonic bath cannot be successfully evaporatively cooled (diamond). However, if bosonic ^{87}Rb (squares) is evaporatively cooled, the fermionic ^{40}K is sympathetically cooled (circles) by thermalizing elastic collisions with ^{87}Rb. The vertical axes indicate the evolution of phase-space density en route to dual quantum degeneracy ($\mathcal{Z} \geq 1$) during evaporation: ^{40}K fugacity $\mathcal{Z}$ on the left, and ^{87}Rb ground-state occupation on the right. A typical run-to-run spread in atom number is indicated on the right-most point; all vertical error bars are smaller than the marker size.

29) A ^{6}Li DFG has been produced in an all-optical setup in as little as 3.5 s [44].

during the initial high-temperature stages of evaporation. Direct measurements of the ^{40}K and ^{87}Rb temperatures indicate that ^{40}K thermalization lags that of ^{87}Rb despite an experimentally optimized RF frequency sweep that is slower at higher temperatures and accelerates at lower temperatures [5].

12.5.2
K-Rb Cross-Thermalization

We have studied the ^{40}K-^{87}Rb inter-species scattering cross-section σ_{KRb} by measuring cross-thermalization rates at temperatures between 10 and 200 μK [5]. We compare the results, shown in Figure 12.4, to the σ_{KRb}-vs.-temperature behavior predicted by two scattering models. The simpler model, assuming only s-wave contact-interaction scattering, predicts $\sigma_{\mathrm{KRb}} = 4\pi a^2/(1 + a^2k^2) > \sigma_{\mathrm{RbRb}}$ throughout the stated temperature range, where $a = a_{\mathrm{KRb}}$ is the ^{40}K-^{87}Rb s-wave scattering length, and k the relative wavevector in the center-of-mass frame. The second more detailed model is based on an effective-range atom–atom scattering theory which includes the next-order correction to the s-wave scattering phase shift [45, 46] and is in good agreement with our measurements.

We attribute the observed reduction in scattering cross-section to the onset of the Ramsauer–Townsend effect, in which the s-wave scattering phase and cross-section approach zero for a particular value of relative energies between particles [5, 47].

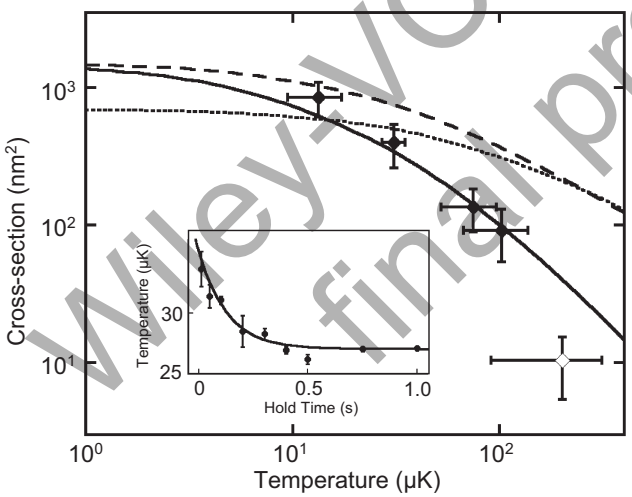

Figure 12.4 K-Rb cross-species thermalization. Measurements of σ_{KRb} (diamonds) are compared with the s-wave-only (dashed) and effective-range (solid) scattering models (see text). For reference, the s-wave σ_{RbRb} is also shown (dotted). Inset: We measure the cross-thermalization by abruptly reducing the temperature of ^{87}Rb and watching the temperature of ^{40}K relax with time. The data shown has an asymptotic ^{40}K temperature of 27 μK. The highest temperature point (open diamond) did not completely thermalize and lies off of the effective range prediction. A more sophisticated analysis may be required for this point, owing to severe trap anharmonicity at this high temperature. The vertical error bars are statistical (one standard deviation); the horizontal error bars show the spread in initial and final ^{40}K temperature during rethermalization.

Despite the high-temperature reduction in cross-section, however, ^{40}K and ^{87}Rb are relatively good sympathetic cooling partners. By comparison, ^{6}Li-^{87}Rb sympathetic cooling measurements [48, 49] suggest a zero-temperature cross-section approximately 100 times smaller than σ_{KRb}; in other words, a maximum ^{6}Li-^{87}Rb cross-section roughly equal to the lowest ^{40}K-^{87}Rb value we measure.

12.5.3 Density-Dependent Loss

The large and negative inter-species scattering length a_{KRb} results in a strong ^{40}K-^{87}Rb attractive interaction. At low temperatures and high atomic densities, this interaction creates an additional mean-field confinement that can lead to massive and sudden losses during sympathetic cooling [40, 41, 43]. These studies of density-dependent interaction-driven losses point to boson-boson-fermion[30] 3-body decay as the underlying mechanism for the collapse of the mixture. This effect ultimately limits the atom numbers in ^{40}K-^{87}Rb mixtures.

These effects manifest themselves in our experiment as ^{40}K and ^{87}Rb number losses near the end of evaporation. While we are able to produce BECs of up to 3×10^5 atoms when we work with ^{87}Rb alone, the simultaneous ^{87}Rb and ^{40}K atom numbers are restricted to at most $\sim 10^5$ and 4×10^4 respectively (see Figure 12.3).

12.5.4 Required Temperature

The reduction in the K-Rb elastic scattering cross-section discussed in Section 12.5.3 may lead the reader to wonder why we started evaporative cooling at such a high temperature. The reason is that the ^{87}Rb-^{87}Rb elastic collision rate required for efficient evaporative cooling within our magnetic trap lifetime imposes a lower bound on the initial temperature. In this section we will shift our focus to *single-species* collision rates in order to understand this constraint.

Evaporative cooling requires a trap lifetime that is some multiple (typically 10^3) of $\gamma_{\mathrm{coll}}^{-1}$, where $\gamma_{\mathrm{coll}} = n_0 \sigma v_{\mathrm{r}}$ is the collision rate at the center of the trap; n_0 is the central density, σ is the elastic scattering cross-section, and $v_{\mathrm{r}} = \sqrt{8 k_{\mathrm{B}} T/\pi M}$ is the relative velocity of collision partners [50].

Since $\rho_0 \approx n_0 \Lambda_{\mathrm{T}}^3$ at the start of evaporation (see Section 12.4.4), we can express the central density in terms of the phase-space density:

$$\gamma_{\mathrm{coll}} = \frac{\sigma \rho_0 M}{\pi^2 \hbar^3} (k_{\mathrm{B}} T)^2 \,, \tag{12.27}$$

which is independent of atom number.

This relation can be used to give a lower bound on temperature in a broad range of traps. Defining $\gamma_{\mathrm{coll}}^{\mathrm{min}}$ as the minimum scattering rate,

$$(k_{\mathrm{B}} T)^2 \geq \gamma_{\mathrm{coll}}^{\mathrm{min}} \frac{\pi^2 \hbar^3}{M \sigma \rho_0} \,. \tag{12.28}$$

30) Fermion-fermion-boson 3-body decay is precluded by the Pauli exclusion principle.

In the case of ^{87}Rb, approximating σ by its low temperature limit $8\pi a_s^2$, where a_s is the s-wave scattering length, we find that the minimum temperature at the beginning of evaporative cooling is

$$T_0^{\min} = 300\,\mu\mathrm{K} \times \left(\frac{10^{-6}}{\rho_0}\right)^{1/2} \left(\frac{\gamma_{\mathrm{coll}}^{\min}}{150\,\mathrm{s}^{-1}}\right)^{1/2}, \tag{12.29}$$

for *any* loaded atom number or trap geometry. In our case, the Rb-Rb elastic collision rate at the start of RF evaporation is roughly $150\,\mathrm{s}^{-1}$, and the phase-space density 10^{-6} or slightly higher. Equation (12.29) predicts $T_0^{\min} = 300\,\mu$K, which exactly coincides with the temperature we measure at the start of evaporation. (The excellent agreement should be taken with a grain of salt, since the model is only approximate.) Can we gain anything by decompressing or compressing the trap? Our trap lifetime $\tau_t \sim 5\,$s is only 750 times larger than the collision time $\gamma_{\mathrm{coll}}^{-1} = 1/150 \simeq 6.7\,$ms – less than optimal, assuming that we require $\tau_t \gtrsim 1000\gamma_{\mathrm{coll}}^{-1}$ for efficient evaporation. Any adiabatic decompression would decrease our collision rate below $\gamma_{\mathrm{coll}}^{\min}$ and result in significant loss of evaporation efficiency. If the trap lifetime were longer, decompression *would* reduce the temperature without sacrificing evaporation efficiency; $\tau_t > 1000\gamma_{\mathrm{coll}}^{-1}$ would be much easier to satisfy even as $\gamma_{\mathrm{coll}}^{-1}$ decreased in the decompression. Compressing the trap near the end of evaporation would increase in K-Rb 3-body loss, which would exacerbate the losses we already observe due to attractive ^{40}K-^{87}Rb interactions near the end of evaporation (see Section 12.5.3). Compressing near the beginning of evaporation should not induce much loss since densities are relatively small at that point, but compression causes dramatic loss in our case due to the limited trap depth. For these reasons, we have little choice but to start our evaporation in the regime where the Ramsauer–Townsend effect is significant.

12.5.5
Experimental Signatures of Fermi Degeneracy

Following the discussion in Section 12.2.3, we assess the degree of Fermi degeneracy in ^{40}K by fitting ideal Boltzmann and Fermi gas theory to time-of-flight absorption data. Unlike the Boltzmann gas, whose spatial width tends toward zero as $T \to 0$, Pauli exclusion results in a finite-sized Fermi gas with a finite average momentum, even at $T = 0$ [27]. This Fermi pressure (see Section 12.2.3) is evident in Figure 12.5a, in which the in-trap cloud width deviates from the Boltzmann prediction for $T/T_F \lesssim 0.5$. Absorption images taken at $T/T_F = 0.95$ and 0.35 are overlayed with a circle indicating E_F in Figure 12.5b,c, demonstrating that the average momentum of the Fermi gas plateaus at low temperature.

In addition to the expansion energy, a second measure of the degree of Fermi degeneracy is the deviation of the time-of-flight spatial profile from the Gaussian envelope predicted by Boltzmann statistics. The Gaussian fit is excellent at high temperatures, but fails at low temperatures [1]. Figure 12.5d shows the residuals of a Gaussian fit using Eq. (12.18) to a gas at $T/T_F = 0.1$, compared to those of a fit

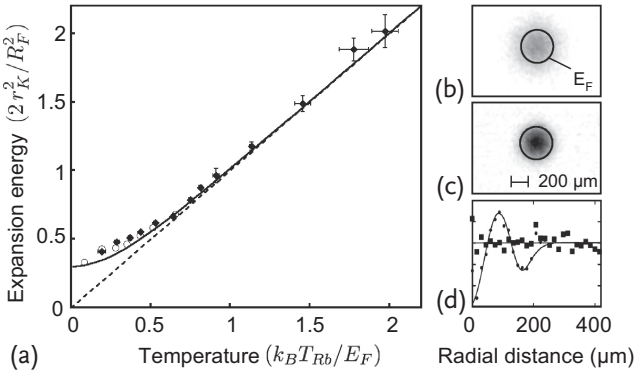

Figure 12.5 (a) The apparent *in situ* fermion temperature measured by Gaussian fits to ^{40}K time-of-flight absorption data, plotted versus temperature of both thermal (diamonds) and Bose-condensed (circles) ^{87}Rb. The data follows a curve derived from Gaussian fits to artificial, perfect Fermi distributions (solid line), deviating from the corresponding Boltzmann prediction (dashed) at temperatures below $T/T_F \approx 0.5$. Quantum degeneracy of ^{87}Rb has little effect on the ^{40}K expansion energy in this data (circles vs. diamonds). (b, c) Absorption images for $T/T_F = 0.95$ and 0.35 respectively, overlayed with black circles of radius R_F rescaled after time-of-flight (see Section 12.2.2). (d) Residuals from radial fits of Gaussian (dots) and Fermi–Dirac (squares) envelope functions to absorption data at $T/T_F = 0.1$. The good Fermi–Dirac fit and poor Gaussian fit are evidence of a Fermi degenerate sample.

using Eq. (12.17), which assumes Fermi–Dirac statistics. Though the Gaussian and Fermi–Dirac profiles are very similar, careful analysis shows that the Fermi–Dirac function is a better fit, with a reduced χ^2 three times lower than the Gaussian fit.

12.6 Species-Selective RF Manipulation

For atoms confined to a magnetic trap, an applied field oscillating at radio frequencies (RF) can resonantly couple adjacent m_F states. The atomic system in the combined static and time-varying magnetic fields can be described by a Hamiltonian with new, uncoupled eigenstates – the so-called "adiabatic" or "RF-dressed" states [51]. The spatial dependence of these states, and thus the spatial character of the trapping potential, can be manipulated by varying the RF amplitude B_{RF} and frequency ω_{RF} (see Chapter 7 for a thorough review of RF-dressed potentials). In this section we discuss two useful regimes for manipulating ultra-cold boson–fermion mixtures on atom chips using these effects.

The first type of RF manipulation is species-selective evaporative cooling. As implied in Section 12.5, RF manipulation can drive ^{87}Rb spin-flip transitions to untrapped spin states at the edge of the ^{87}Rb dressed potential without inducing loss in ^{40}K, as a consequence of the explicit m_F and g_F dependence of the magnetic trapping potentials. In the second type of RF manipulation, B_{RF} is large enough that Landau–Zener tunneling between dressed states is suppressed and the usual adiabatic condition is satisfied [50]. Atoms adiabatically follow the RF-dressed mag-

netic eigenstates and remain trapped in a double-well potential [52–54]. This effect was first demonstrated on both thermal [51, 55] and quantum degenerate Bose gases [11, 56] and is now a well-established method for dynamically "splitting" an ultra-cold Bose gas [11–14, 57]. We have added to this work by demonstrating the simultaneous creation of a ^{87}Rb double well and a ^{40}K single well [15]. This result demonstrates that the adiabatic potentials experienced by each species can be dramatically different in an applied RF field, owing to the different values of g_F for ^{87}Rb and ^{40}K.

12.6.1 Sympathetic RF Evaporation

In this section we consider a simple sympathetic cooling scenario, typical in our experiments; an RF "knife" is used to evaporatively cool ^{87}Rb, which then acts as a refrigerant for the ^{40}K.[31] Ideally, this scheme would causes no loss of ^{40}K atoms; here we explore to what extent this is true.

A critical parameter in evaporative cooling is $\eta = U_{td}/k_B T$ (see Section 12.4.2). The larger the choice of η, the fewer atoms are removed from the trap, since a smaller fraction of the kinetic energy distribution lies above U_{td} [50]. In sympathetic cooling of ^{40}K by ^{87}Rb, we would ideally like the RF field to have no effect on the ^{40}K trap depth. However, we shall see that for our scheme the RF knife *does* limit the trap depth for ^{40}K, though the effect is small. This effect may be quantified by evaluating η for ^{40}K in our cooling scheme.

We begin by considering atoms in spin states $|F, m_F\rangle$ in a static ("DC") magnetic trap, whose potential is $U(\boldsymbol{r}) = m_F g_F \mu_B B_{DC}(\boldsymbol{r})$. The minimum magnetic field amplitude is $B_0 \equiv B_{DC}(0)$ using the notation $B_{DC}(\boldsymbol{r}) \equiv |\boldsymbol{B}_{DC}(\boldsymbol{r})|$. We apply a weak, sinusoidally time-varying magnetic field of amplitude B_{RF} and frequency ω_{RF}. If $\hbar\omega_{RF} > g_F \mu_B B_0$, then atoms in state m_F at positions $\boldsymbol{r}_1$ for which

$$g_F \mu_B B_{DC}(\boldsymbol{r}_1) = \hbar\omega_{RF} \tag{12.30}$$

can undergo spin-flips to adjacent m_F states, including untrapped ones. This imposes an effective trap depth $U_{td} = g_F m_F \mu_B (B_{DC}(\boldsymbol{r}_1) - B_0)$ on these atoms, since any atom with energy above U_{td} is ejected from the trap. Therefore, we can write

$$U_{td} \equiv \eta k_B T = m_F(\hbar\omega_{RF} - g_F \mu_B B_0) \tag{12.31}$$

for a gas of atoms in state $|F, m_F\rangle$ in thermal equilibrium at temperature T.

For two species in thermal equilibrium in the same magnetic trap, we can write down simultaneous equations like (12.31) for both species. From these, we infer the relationship

$$\eta_K = \left(\frac{m_F^{(K)}}{m_F^{(Rb)}}\right)\eta_{Rb} + m_F^{(K)}\left[g_F^{(Rb)} - g_F^{(K)}\right]\frac{\mu_B B_0}{k_B T}\,. \tag{12.32}$$

31) Microwave magnetic fields at 6.8 GHz may also be used to species-selectively evaporate ^{87}Rb via hyperfine transitions [48].

between the two η parameters in the case of ^{40}K and ^{87}Rb, using the fact that ω_{RF} and B_0 are common to both species. This convenient form highlights the role of m_F and g_F in the RF evaporation of a mixture of atomic species.

Moving now to a more specific case, we note that typical sympathetic cooling ramps are done with ^{87}Rb in the $|2, 2\rangle$ state, and the ^{40}K in $|9/2, 9/2\rangle$, since this mixture is stable with respect to many inelastic collisions [40]. Equation (12.32) yields

$$\eta_K = \frac{9}{4}\eta_{Rb} + \frac{5}{4}\frac{\mu_B B_0}{k_B T} , \tag{12.33}$$

from which we immediately conclude that $\eta_K > 9\eta_{Rb}/4$ for all values of temperature. Having $\eta_K > \eta_{Rb}$ ensures that ^{87}Rb can be evaporated without inducing significant loss in the ^{40}K population, as required for efficient sympathetic evaporative cooling.

For a typical experimental value of $\eta_{Rb} \approx 8$, which is roughly constant throughout the evaporation, Figure 12.6 demonstrates that η_K rises sharply for all trappable $m_F^{(K)}$ states as sympathetic evaporation proceeds and the ^{40}K temperature decreases. ^{40}K spin-flip losses are most likely to occur when η_K is smallest. In our experiments, this occurs at the beginning of evaporation, when $B_0 = 5.7$ G, $T \sim 300$ μK [5, 15], and $\eta_K = 8.1$.

We can also use Eq. (12.33) to compare η_K and η_{Rb} in the scenario in which all the ^{87}Rb is evaporated away to leave a pure ^{40}K DFG. Taking $\eta_{Rb} \to 0$ and working at a typical pure-DFG temperature $T = 220$ nK [5], we find $\eta_K > 220$ for all trappable ^{40}K sublevels. This confirms that ^{87}Rb can be fully and selectively ejected from the trap without causing any significant ^{40}K loss.

Finally, we note that it is possible in principle to evaporate ^{40}K without inducing ^{87}Rb loss. For RF frequencies $\hbar\omega_{RF} \leq g_F^{(Rb)}\mu_B B_0$, only ^{40}K atoms are ejected from the trap, at positions r_2 such that $\hbar\omega_{RF} = g_F^{(K)}\mu_B B(r_2)$. Following the derivation of Eq. (12.31), we can express the ^{40}K trap depth in this scenario

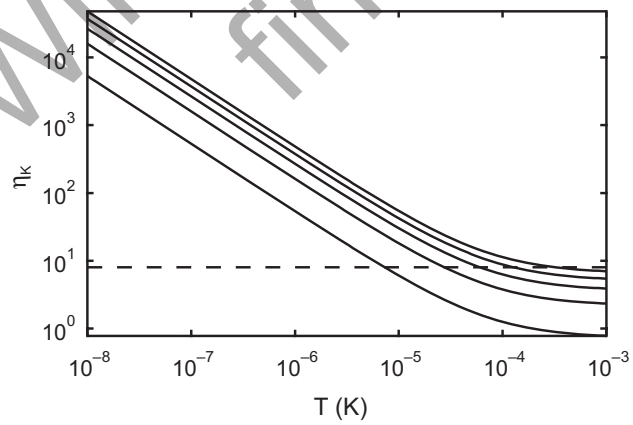

Figure 12.6 Evaporation parameter η_K for ^{40}K atoms in a typical sympathetic cooling ramp with $B_0 = 5.7$ G and $\eta_{Rb} \approx 8$ (dashed line, see text). The curves represent different magnetically trappable values of $m_F^{(K)}$ (1/2 to 9/2, from bottom to top). η_K rises sharply as evaporation proceeds and the temperature decreases, while η_{Rb} remains constant.

as $U_{\rm td}^{(\rm K)} = m_{\rm F}^{(\rm K)}[g_{\rm F}^{(\rm Rb)} - g_{\rm F}^{(\rm K)}]\mu_{\rm B} B_0$. In our experiment, using $B_0 = 5.7\,\rm G$ and the stretched states of ^{40}K and ^{87}Rb, $U_{\rm td} = 5\mu_{\rm B} B_0/4 \simeq k_{\rm B} \times 480\,\mu\rm K$. Thus, we expect to be able to evaporate $T \lesssim 480\,\mu\rm K$ ^{40}K clouds without affecting the ^{87}Rb population.

12.6.2 Species-Selective Double Wells

In this section we discuss the species-selective nature of RF-dressed double wells. In a two-species mixture, this effect permits the simultaneous formation of a double-well potential for ^{87}Rb and single-well potential for ^{40}K [15], and vice versa. We use an RF amplitude $B_{\rm RF} \ll B_0$, for which the effective adiabatic potentials[32] may be written [11–13]

$$U_{\rm eff}(\boldsymbol{r}) = m'_{\rm F}\sqrt{\delta(\boldsymbol{r})^2 + \Omega(\boldsymbol{r})^2} \tag{12.34}$$

where

$$\begin{aligned} \delta(\boldsymbol{r}) &= \mu_{\rm B} g_{\rm F} B_{\rm DC}(\boldsymbol{r}) - \hbar\omega_{\rm RF} \\ \Omega(\boldsymbol{r}) &= \mu_{\rm B} g_{\rm F} B_{\rm RF\perp}(\boldsymbol{r})/2\,, \end{aligned} \tag{12.35}$$

$B_{\rm DC}(\boldsymbol{r}) \equiv |\boldsymbol{B}_{\rm DC}(\boldsymbol{r})|$ is the static magnetic field amplitude, $B_{\rm RF\perp}(\boldsymbol{r})$ is the amplitude of the $B_{\rm RF}$ component which is perpendicular to $\boldsymbol{B}_{\rm DC}(\boldsymbol{r})$ at point $\boldsymbol{r}$, and $m'_{\rm F}$ is the new, effective magnetic quantum number. The parameters $\delta(\boldsymbol{r})$ and $\Omega(\boldsymbol{r})$ can be identified as the local detuning and Rabi frequency of the RF field, respectively. Using Eq. (12.34), we can calculate effective adiabatic potentials for ^{87}Rb and ^{40}K and use them to illustrate the simultaneous creation of single- and double-well potentials in a ^{40}K-^{87}Rb mixture.

For clarity, we consider the formation of the ^{87}Rb double well and ^{40}K single well separately. Our starting point is a $|9/2, 9/2\rangle$–$|2, 2\rangle$ ^{40}K-^{87}Rb mixture confined to a static, anisotropic harmonic Z-trap directly above the RF wire (see Figure 12.7a) with $B_0 = 1.214\,\rm G$, $\omega_{x,z} = 2\pi \times 1.23\,\rm kHz$, and $\omega_y = 2\pi \times 13.7\,\rm Hz$.

Rb Double Well An RF field with initial frequency $\omega_{\rm RF} = 2\pi \times 800\,\rm kHz$ and detuning $\delta^{(\rm Rb)} = -50\,\rm kHz$ is applied by ramping up its amplitude from zero to the final value $B_{\rm RF} = 200\,\rm mG$. A potential barrier is formed at $\boldsymbol{r} = 0$ by sweeping the RF frequency through the resonant point $\delta^{(\rm Rb)}(0) = 0$. As the RF field is applied,

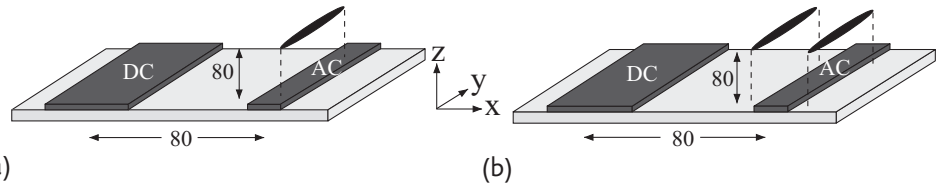

Figure 12.7 Atoms confined to single-well (a) and double-well (b) potentials induced by RF manipulation 80 μm above the chip surface.

32) For $B_{\rm RF} \approx B_0$, Eq. (12.34), which relies on the rotating-wave approximation (RWA), is no longer valid [53, 54, 58].

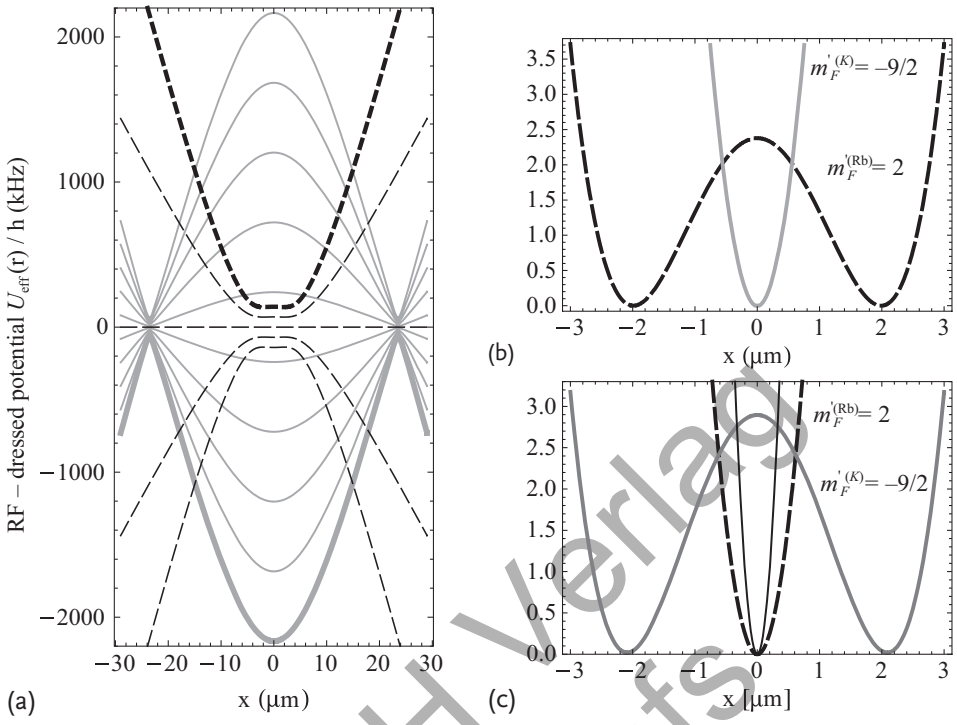

Figure 12.8 Simultaneous adiabatic dressed potentials for ^{87}Rb and ^{40}K. (a) The ^{87}Rb-double-well case. ^{87}Rb (black) and ^{40}K (gray) effective dressed potentials are plotted as a function of the spatial coordinate x (see Figure 12.7). Each curve corresponds to a single value of m'_F for ^{87}Rb and ^{40}K, with the upper-most curves corresponding to $m'_F = 2$ and $m'_F = 9/2$, respectively. ^{87}Rb atoms populate their upper-most $m'_F = 2$ dressed state (thick, dashed), while ^{40}K atoms populate their lower-most $m'_F = -9/2$ single-well dressed state (thick, gray). (b) A closer view of the ^{87}Rb double well and ^{40}K single well, plotted together on a single vertical U_{eff}/h axis in units of kHz. Both curves have been shifted vertically to align their potential minima at zero kHz. (c) A closer view of the ^{40}K double well and ^{87}Rb single well, with vertical axis similar to (b). The dressed ^{87}Rb single well (black, dashed) deviates slightly from the undressed single well (solid, thin black), illustrating the slight loss of radial trap curvature.

each undressed state is adiabatically connected to one dressed state; here $m_F^{(Rb)} = 2$ is connected to $m_F'^{(Rb)} = 2$, shown as the upper-most black curve in Figure 12.8a. After sweeping to a final RF frequency $\omega_{RF} = 2\pi \times 860\,\text{kHz}$, the barrier height is $h \times 2.4\,\text{kHz}$ and the x-direction double-well separation is $4\,\mu$ (see Figure 12.8b). The $m_F'^{(Rb)}$ level repulsion at the double-well minima is 70 kHz, sufficient to prevent Landau–Zener spin-flips at our working temperatures $T \lesssim 1\,\mu\text{K}$. The ^{87}Rb population thus remains trapped in the $m_F'^{(Rb)} = 2$ dressed level.

K Single Well The trapping potential for the ^{40}K atoms is affected in a very different way for the same magnetic field configuration. In our current example (Figure 12.8a,b), the detuning for ^{40}K is positive; $\delta^{(K)}(0) = 2\pi \times 482\,\text{kHz}$ at the trap minimum. Near $\boldsymbol{r} = 0$, the RF dressing adiabatically connects $m_{F(K)} = 9/2$ to $m_{F'}^{(K)} = -9/2$. Since $[\delta^{(K)}(0)]^2 \gg [\Omega^{(K)}(0)]^2$, the potential curvature near $\boldsymbol{r} = 0$

is largely unaffected by the RF coupling (see Eq. (12.34)). More quantitatively, the dressed states are most deformed where $\delta^{(K)}(\boldsymbol{r}) \approx 0$, which corresponds to $x \simeq \pm 23\,\mu\text{m}$, and a potential energy of roughly 110 μK above the local minimum at $\boldsymbol{r} = 0$. Since our experiments are typically conducted with $T \lesssim 1\,\mu\text{K}$, we can be satisfied that the ^{40}K potential retains its original form near $\boldsymbol{r} = 0$ without inducing any ^{40}K loss.

One important feature of this single- and double-well arrangement is that the ^{87}Rb double-well separation and barrier height may be tuned over a wide range by adjusting ω_{RF} and B_{RF} without affecting the shape of the ^{40}K potential.

An obvious extension of the work described here and in [15] would be to reverse the roles of boson and fermion, creating a double well for fermions overlapped with a single well for bosons. The magnetic hyperfine structure of ^{40}K and ^{87}Rb makes this possible in a ^{40}K-^{87}Rb mixture, but with slightly different results than in the ^{87}Rb-double-well case.

Following the ^{87}Rb-double-well example of the preceding section, here we sweep the RF frequency from $\omega_{\text{RF}} = 2\pi \times 338\,\text{kHz}$ to $\omega_{\text{RF}} = 2\pi \times 383\,\text{kHz}$. In the same static trap with $B_0 = 1.214\,\text{G}$, $\delta^{(K)}$ changes sign from -50 to $+5\,\text{kHz}$, while $\delta^{(\text{Rb})}$ remains negative throughout. This creates a ^{40}K double well in the $m_{\text{F}}^{\prime(K)} = 9/2$ state with x-direction well separation $\sim 4\,\mu\text{m}$, barrier height $h \times 2.9\,\text{kHz}$ at $\boldsymbol{r} = 0$, and $m_{\text{F}}^{\prime(K)}$ level repulsion $\sim 70\,\text{kHz}$ at $x = \pm 2.1\,\mu\text{m}$. In contrast to the ^{87}Rb-double-well scenario, here *both* ^{40}K and ^{87}Rb adiabatically follow their respective uppermost dressed levels, which exhibit their strongest spatial deformation near the trap center. While ^{40}K experiences a double-well potential, the ^{87}Rb $m_{\text{F}}^{\prime(\text{Rb})} = 2$ potential is a single well with slightly reduced radial curvature from the initial, undressed $m_{\text{F}} = 2$ potential, as shown in Figure 12.8c.

In addition to the species-selectivity of this process, it should be emphasized that atom chips are particularly well-suited to creating adiabatic dressed-state potentials due to the proximity of the atoms to chip wire RF antennae. The double wells described in this section were created using RF Rabi frequencies $\Omega \sim 100\text{–}200\,\text{kHz}$, though we can achieve values as large as 1 MHz with tens of milliamperes rms in the chip wire antenna. By comparison, achieving $\Omega \approx 1\,\text{MHz}$ with an air-side RF antenna would require a circular coil of radius 3 cm and 3 turns bearing 10 A rms of AC current.

12.7
Fermions in an Optical Dipole Trap near an Atom Chip

In our discussion of fermions on atom chips thus far, we have focused on spin-polarized ^{40}K in magnetic traps. In this section we describe an extension of our atom chip capabilities with the incorporation of an external crossed-beam optical dipole trap skimming the surface of the atom chip. (See Chapter 3 for a discussion of other on-chip optical potentials.) Optical trapping enables the use of any and all hyperfine and Zeeman spin states in our experiments, as well as more flexible control of the magnetic field environment. These added features allow us to work

with strongly interacting ^{40}K spin mixtures, while retaining the atom chip benefits of near-field RF and microwave manipulation and rapid evaporation to Fermi degeneracy.

12.7.1 Optical Trap Setup

Two optical trapping beams are generated using the output of a single 500-mW Nd:YAG laser operating at $\lambda = 1064$ nm, and directed along the x- and y-directions through the vacuum cell and beneath the atom chip using air-side optics (see Figure 12.9). Ideally, the foci would be near enough to the chip surface to allow sufficient RF and microwave coupling, but not so near that the optical potential is degraded by light scattering off the edges of the chip as the beams are focussed. The beams should also be aligned to the existing Z-trap position for efficient transfer from the Z-trap into the dipole trap. To satisfy these constraints we focus the two beams at roughly 190 μ beneath the chip surface, with $1/e^2$ waists $w_0 \sim 18$ and 30 μm, and Rayleigh ranges $z_0 = \pi w_0^2/\lambda \sim 1.0$ and 2.7 mm, respectively, as shown in Figures 12.9b,c.

12.7.2 Loading the Optical Trap

We load the optical trap by ramping off the Z-trap magnetic fields and ramping on the optical beams one at a time. First, the y-direction peak beam intensity is

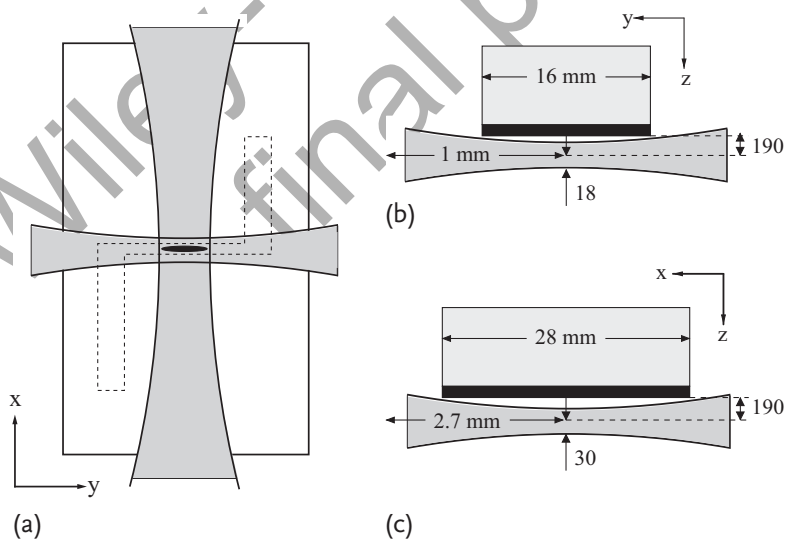

Figure 12.9 Alignment of the dipole beams to the atom chip. (a) Bottom view, showing the alignment with the Z-wire and the trapped atoms (black ellipse). (b, c) Side-views of beams skimming 190 μm below the atom chip surface. Beam waists and Rayleigh ranges are indicated, along with the outer dimensions of the atom chip (black) and copper mounting block (light gray). Dimensions are in units of micrometers unless otherwise indicated.

increased linearly from 0 to $\sim 2.9 \times 10^7$ mW/cm^2 in 100 ms. The Z-trap is then ramped off in 50 ms. Finally, the x-direction peak beam intensity is linearly ramped from 0 to $\sim 8.5 \times 10^6$ mW/cm^2 in 100 ms.

Unlike when loading the Z-trap from the macroscopic magnetic trap (see Section 12.4.1), the mode matching between the Z-trap and the initial single-beam optical trap is excellent. This allows us to load the optical trap with no observable loss in atom number, but not without introducing some heating: 6×10^3 atoms in the Z-trap at $T/T_F \simeq 0.56$ are all transferred into the optical trap, after which $T/T_F \simeq 1$.

12.7.3
Microwave and RF Manipulation

With the atoms now trapped solely by the optical trap, we can use the antenna wire (see Section 12.3.1) to apply microwave radiation with amplitude B_μ and frequency $\omega_\mu \sim 2\pi \times 1.3$ GHz to drive transitions between ^{40}K hyperfine ground states. To test and calibrate our microwave system, however, we first observed the effects of microwave radiation on magnetically trapped ^{40}K. By scanning the microwave frequency near 1.3 GHz in a Z-trap with magnetic minimum $B_0 = 5.22$ G, we observe a loss feature in the trapped atom number, corresponding to hyperfine transitions between the initial trapped state $|9/2, 9/2\rangle$ and the final, untrapped $|7/2, 7/2\rangle$ state (see Figure 12.10a).

Microwave and RF manipulation also allow us to create an interacting Fermi gas in the optical trap with a $|9/2, -9/2\rangle - |9/2, -7/2\rangle$ spin mixture after loading a spin-polarized sample from the Z-trap in state $|9/2, 9/2\rangle$. Atoms are transferred from $|9/2, 9/2\rangle$ to $|9/2, -7/2\rangle$ by rapid adiabatic transfer. In a 20-G external magnetic bias field, we sweep the microwave frequency from below the $|9/2, 9/2\rangle \rightarrow |7/2, 7/2\rangle$ transition ($\omega_\mu = 2\pi \times 1235.8$ MHz) to above the $|7/2, -7/2\rangle \rightarrow |9/2, -7/2\rangle$ transition ($\omega_\mu = 2\pi \times 1336.2$ MHz) in 500 ms. This is followed by a 5-ms RF frequency

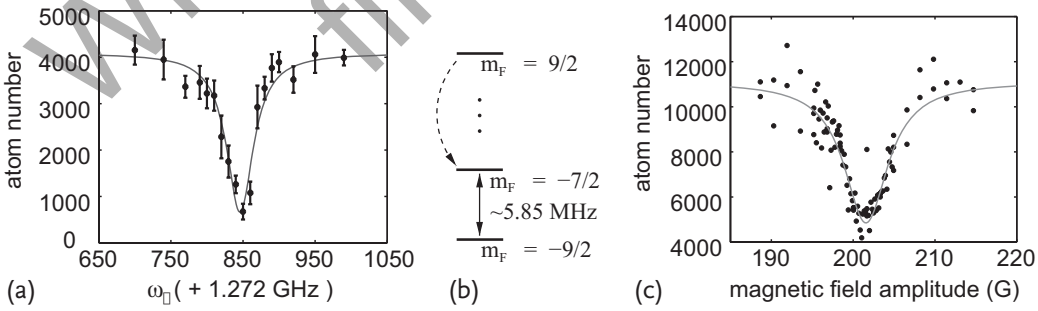

Figure 12.10 (a) Microwave-induced atom number ^{40}K loss from a magnetic Z-trap. (b) Schematic Zeeman level diagram of the ^{40}K $F = 9/2$ hyperfine ground state, indicating the microwave adiabatic rapid population transfer (dashed arrow) and RF pulse (solid arrow) used to create a $|9/2, -7/2\rangle - |9/2, -9/2\rangle$ spin mixture (see text). (c) 3-body loss of spin-mixed ^{40}K from an optical trap is due to an enhancement of the scattering cross-section induced by the Feshbach resonance near 202 G.

sweep from $\omega_{RF} = 2\pi \times 5.80\,\text{MHz}$ to $2\pi \times 5.90\,\text{MHz}$ (see Figure 12.10b), creating an equal spin mixture of $|9/2, -9/2\rangle$ and $|9/2, -7/2\rangle$.

The ^{40}K-^{40}K interaction strength may be dramatically increased using the well-known Feshbach resonance in a DC magnetic field of roughly 202 G [59]. Using external coils, we apply a magnetic bias field and monitor the ^{40}K population as a function of this field. We have observed the Feshbach resonance in our atom chip setup as a strong loss feature near 202 G, as shown in Figure 12.10b. The atom number loss is attributed to 3-body decay induced by the strong interactions near the Feshbach resonance.

12.8 Discussion and Future Outlook

The union of Fermi gases and atom chips is an important step forward in degenerate quantum gas research. In this chapter, we have described our work producing the first DFG on an atom chip. Using a large dual-species MOT, ^{40}K and ^{87}Rb are captured and loaded onto an atom chip in numbers large enough to enable sympathetic evaporative cooling to DFG and dual DFG-BEC quantum degeneracy. The strong confinement and large inter-species collision rate afforded by the micro-magnetic trap permits an evaporation to quantum degeneracy in as little as 6 s, faster than had been previously possible in magnetic traps. We have also demonstrated species-selective double-well potentials in a ^{40}K-^{87}Rb mixture, as well as the creation of a strongly interacting ^{40}K DFG in a crossed-beam optical dipole trap skimming the surface of the atom chip.

We also note several disadvantages associated with using micro-magnetic traps for fermions. Magnetic traps are not ideal for working with the spin-mixtures required for an interacting DFG, since spin-changing collisions can populate magnetically untrapped spin states, causing loss. We address this limitation by incorporating a crossed-beam optical dipole trap into our atom chip setup. The relatively small trap volumes of microtraps also limits the number of target ^{40}K and refrigerant ^{87}Rb atoms that can be loaded into the chip trap. Even at our maximum achievable trap depth, these limits on the number of refrigerant atoms ultimately limit the DFG to 4×10^4 atoms at $T/T_F \gtrsim 0.1$ in our system. By comparison, larger, colder, interacting DFGs are routinely produced in spin-independent optical potentials [2].

Despite these drawbacks, atom chips remain a useful and versatile tool for ultracold Fermi gas research. We close this chapter with descriptions of some of our ongoing and future research directions with a new atom chip: double-well potentials; interacting DFGs and DFG-BEC mixtures; and optical probes and traps.

New Atom Chip We have recently adopted a richer atom chip design, which improves on its predecessor (described in Section 12.3) in three important areas. First, the new conductor layout allows a wider selection of micro-magnetic traps with greater tunability of the oscillation frequencies. We are also now able to generate

RF double-well potentials at arbitrary angles and distances from the chip surface, as in [12]. Second, new near-field antenna wire geometries and high-frequency electrical feedthroughs improve microwave and RF impedance matching, reducing coupling losses between the air-side and the chip. Finally, all electrical connections to the chip are made on the back side of the substrate, increasing the optical access for probe and trapping beams compared to its predecessor. Designed and fabricated at the University of Toronto [60], the chip consists primarily of silver conductors that were patterned by photolithography and evaporatively deposited onto an aluminum nitride substrate.

Bose–Fermi Mixtures and Double-Well Potentials The species-selectivity of RF-dressed double-well potentials may be useful in studying boson–fermion interactions in ultra-cold atomic mixtures. The strong attractive interaction between ^{40}K and ^{87}Rb, known to impede sympathetic cooling in ^{40}K-^{87}Rb mixtures, depends on the inter-species collision rate and related peak ^{40}K and ^{87}Rb number densities [5, 40, 41, 43]. Adiabatic RF manipulation could be used to reduce the ^{87}Rb peak density by decompressing the $m_F'^{(Rb)} = 2$ effective potential at the center of the trap during sympathetic RF evaporation. Ideally, the RF-dressed ^{40}K-^{87}Rb collision rate would be small enough to avoid a density-driven collapse, but still large enough to maintain good inter-species rethermalization for sympathetic cooling.

These potentials are also amenable to the study of phase coherence in the ^{40}K-^{87}Rb mixture as the potential barrier is raised. Recent studies of phase-coherent RF splitting of ^{87}Rb BECs on atom chips [11, 12, 14] and in optical traps [61, 62] have focused on interactions and tunneling in BEC-in-double-well systems. An interesting extension of this work would be to assess the effects of a background, unsplit fermion "bath" on the tunneling dynamics and coherence properties of this system.

Light Scattering by a DFG An inhibition of optical scattering is predicted to occur in DFGs when $E_F \gtrsim E_R$, where E_R is the recoil energy [63, 64]. The optical scattering rate depends on the availability of atomic recoil states ("final states"), which is constrained due to Pauli blocking in the filled or nearly filled Fermi sea of a trapped DFG. The large oscillation frequencies and Fermi energies available in anisotropic, harmonic atom chip microtraps ($E_F \propto \bar{\omega}$, see Section 12.2.1) offer a promising route toward measurements of this effect (see [65] and references therein).

References

1 DeMarco, B. and Jin, D.S. (1999) Onset of Fermi degeneracy in a trapped atomic gas. *Science* **285**, 1703.

2 Bloch, I., Dalibard, J., and Zwerger, W. (2008) Many-body physics with ultracold gases. *Rev. Mod. Phys.* **80**, 885.

3 Ott, H., Fortágh, J., Schlotterbeck, G., Grossmann, A., and Zimmermann, C. (2001) Bose–Einstein condensation in a surface microtrap. *Phys. Rev. Lett.* **87**, 230401.

4 Hänsel, W., Hommelhoff, P., Hänsch, T.W., and Reichel, J. (2001) Bose–

Einstein condensation on a microelectronic chip. *Nature* **413**, 498.
5 Aubin, S., Myrskog, S., Extavour, M.H.T., LeBlanc, L.J., McKay, D., Stummer, A., and Thywissen, J.H. (2006) Rapid sympathetic cooling to Fermi degeneracy on a chip. *Nat. Phys.* **2**, 384.
6 Mathey, L., Wang, D.W., Hofstetter, W., Lukin, M.D., and Demler, E. (2004) Luttinger liquid of polarons in one-dimensional boson-fermion mixtures. *Phys. Rev. Lett.* **93**, 120404.
7 Rauf, H., Pichler, T., Knupfer, M., Fink, J., and Kataura, H. (2004) Transition from a Tomonaga-Luttinger liquid to a Fermi liquid in potassium-intercalated bundles of single-wall carbon nanotubes. *Phys. Rev. Lett.* **93**, 096805.
8 Lieb, E.H. (1966) *Mathematical Physics in One Dimension: Exactly Soluble Models of Interacting Particles,* Perspectives in physics, Academic Press, New York, NY.
9 Moritz, H., Stöferle, T., Günter, K., Köhl, M., and Esslinger, T. (2005) Confinement induced molecules in a 1D Fermi gas. *Phys. Rev. Lett.* **94**, 210401.
10 Recati, A., Fedichev, P.O., Zwerger, W., and Zoller, P. (2003) Fermi one-dimensional quantum gas: Luttinger liquid approach and spin-charge separation. *J. Opt.B: Quantum Semiclass. Opt.* **5**, S55.
11 Schumm, T., Hofferberth, S., Wildermuth, L.M., Groth, S., Bar-Joseph, I., Schmiedmayer, J., and Krüger, P. (2005) Matter–wave interferometry in a double well on an atom chip. *Nat. Phys.* **1**, 57.
12 Hofferberth, S., Lesanovsky, I., Fischer, B., Verdu, J., Schmiedmayer, J., and Krüger, P. (2006) Radio-frequency dressed state potentials for neutral atoms. *Nat. Phys.* **2**, 710.
13 Lesanovsky, I., Schumm, T., Hofferberth, S., Andersson, L.M., Krüger, P., and Schmiedmayer, J. (2006) Adiabatic radio-frequency potentials for the coherent manipulation of matter waves. *Phys. Rev. A* **73**, 033619.
14 Jo, G.B., Will, S., A. Pasquini, T., Saba, M., Ketterle, W., and Pritchard, D.E. (2007) Long phase coherence time and number squeezing of two Bose–Einstein condensates on an atom chip. *Phys. Rev. Lett.* **98**, 030407.
15 Extavour, M.H.T., LeBlanc, L.J., Schumm, T., Cieslak, B., Myrskog, S., Stummer, A., Aubin, S., and Thywissen, J.H. (2006) *Dual-species quantum degeneracy of ^{40}K and ^{87}Rb on an atom chip,* in *Atomic Physics, Proceedings of the 20th International Conference on Atomic Physics* (eds C. Roos, H. Häffner, and R. Blatt), vol. 20, 241–249, American Institute of Physics.
16 Yurke, B. (1986) Input states for enhancement of fermion interferometer sensitivity. *Phys. Rev. Lett.* **56**, 1515.
17 Das, K. and Aubin, S. (2008) *Mesoscopic quantum pumping circuit simulations,* Manuscript in preparation.
18 Jeltes, T., McNamara, J.M., Hogervorost, W., Vassen, W., Krachmalnicoff, V., Schellekens, M., Perrin, A., Chang, H., Boiron, D., Aspect, A., and Westbrook, C.I. (2007) Comparison of the Hanbury Brown–Twiss effect for bosons and fermions. *Nature* **445**, 402.
19 Tran, M.N., Murthy, M.V.N., and Bhaduri, R.K. (2001) Ground-state fluctuations in finite Fermi systems. *Phys. Rev. E* **63**, 031105.
20 Tran, M.N. (2003) Exact ground-state number fluctuations of trapped ideal and interacting fermions. *J. Phys. A: Math. Gen.* **36**, 961.
21 Budde, M. and Mølmer, K. (2004) Number distributions for fermions and fermionized bosons in periodic potentials. *Phys. Rev. A* **70**, 053618.
22 Wang, Y.J., Anderson, D.Z., Bright, V.M., Cornell, E.A., Diot, Q., Kishimoto, T., Prentiss, M., Saravanan, R.A., Segal, R., and Wu, S. (2005) Atom Michelson interferometer on a chip using a Bose–Einstein condensate. *Phys. Rev. Lett.* **94**, 090405.
23 Colombe, Y., Steinmetz, T., Dubois, G., Linke, F., Hunger, D., and Reichel, J. (2007) Strong atom-field coupling for Bose–Einstein condensates in an optical cavity on a chip. *Nature* **450**, 272.
24 Castin, Y. (2008) *Trapped Fermi Gases,* in *Proceedings of the International School of Physics Enrico Fermi* (eds M. Inguscio,

W. Ketterle, and C. Salomon), vol. 164, 289–349, IOS Press.
25 Bruun, G.M. and Clark, C.W. (2000) Ideal gases in time-dependent traps. *Phys. Rev. A* **61**, 061601.
26 Pathria, R.K. (1996) *Statistical Mechanics, 2nd ed.*, Butterworth Heineman, Woburn, MA.
27 Truscott, A.G., Strecker, K.E., McAlexander, W.I., Partridge, G.B., and Hulet, R.G. (2001) Observation of Fermi Pressure in a Gas of Trapped Atoms. *Science* **291**, 2570.
28 Butts, D.A. and Rokhsar, D.S. (1997) Trapped Fermi gases. *Phys. Rev. A* **55**, 4346.
29 Reichel, J. and Thywissen, J. (2004) Using magnetic chip traps to study Tonks–Girardeau quantum gases. *J. Phys. IV France* **116**, 265.
30 Estève, J. (2004) *Du miroir au guide d'onde atomique: effets de rugosité*, Ph.D. thesis, Laboratoire Charles Fabry de Institut d'Optique, Université Paris IV.
31 Aussibal, C. (2003) *Réalisation d'un condensat de Bose–Einstein sur une microstructure*, Ph.D. thesis, Laboratoire Charles Fabry, L'Université Paris IV Université Paris IV.
32 Aubin, S., Extavour, M.H.T., Myrskog, S., LeBlanc, L.J., Estève, J., Singh, S., Scrutton, P., McKay, D., McKenzie, R., Leroux, I.D., Stummer, A., and Thywissen, J.H. (2005) Trapping fermionic ^{40}K and bosonic ^{87}Rb in a chip trap. *J. Low Temp. Phys.* **140**, 377.
33 Extavour, M.H.T. (2004) *Design and construction of magnetic trapping and transport elements for neutral atoms*, Master's thesis, Department of Physics, University of Toronto.
34 Reichel, J. (2002) Microchip traps and Bose–Einstein condensates. *Appl. Phys. B* **75**, 469.
35 Estève, J., Aussibal, C., Schumm, T., Figl, C., Mailly, D., Bouchoule, I., Westbrook, C.I., and Aspect, A. (2004) Role of wire imperfections in micromagnetic traps for atoms. *Phys. Rev. A* **70**, 043629.
36 Schumm, T., Estève, J., Figl, C., Trebbia, J.B., Aussibal, C., Nguyen, H., Mailly, D., Bouchoule, I., Westbrook, C.I., and Aspect, A. (2005) Atom chips in the real world: the effects of wire corrugation. *Eur. Phys. J. D* **32**, 171.
37 Reichel, J., Hänsel, W., and Hänsch, T.W. (1999) Atomic micromanipulation with magnetic surface traps. *Phys. Rev. Lett.* **83**, 3398.
38 Luiten, O.J., Reynolds, M.W., and Walraven, J.T.M. (1996) Kinetic theory of the evaporative cooling of a trapped gas. *Phys. Rev. A* **53**, 381.
39 Weinstein, J.D. and Libbrecht, K.G. (1995) Microscopic magnetic traps for neutral atoms. *Phys. Rev. A* **52**, 4004.
40 Roati, G., Riboli, F., Modugno, G., and Inguscio, M. (2002) Fermi–Bose quantum degenerate ^{40}K-^{87}Rb mixture with attractive interaction. *Phys. Rev. Lett.* **89**, 150403.
41 Modugno, G., Roati, G., Riboli, F., Ferlaino, F., Brecha, R., and Inguscio, M. (2002) Collapse of a degenerate fermi gas. *Science* **297**, 2240.
42 Goldwin, J., Inouye, S., Olsen, M.L., Newman, B., DePaola, B.D., and Jin, D.S. (2004) Measurement of the interaction strength in a Bose–Fermi mixture with ^{87}Rb and ^{40}K. *Phys. Rev. A* **70**, 021601.
43 Ospelkaus, C., Ospelkaus, S., Sengstock, K., and Bongs, K. (2006) Interaction-driven dynamics of ^{40}K/^{87}Rb Fermi–Bose gas mixtures in the large-particle-number limit. *Phys. Rev. Lett.* **96**, 020401.
44 O'Hara, K.M., Hemmer, S.L., Gehm, M.E., Granade, S.R., and Thomas, J.E. (2002) Observation of a strongly interacting degenerate fermi gas of atoms. *Science* **298**, 2179.
45 Flambaum, V.V., Fribakin, G.F., and Harabati, C. (1999) Analytical calculation of cold-atom scattering. *Phys. Rev. A* **59**, 1998.
46 Anderlini, M., Courtade, E., Cristiani, M., Cossart, D., Ciampini, D., Sias, C., Morsch, O., and Arimondo, E. (2005) Sympathetic cooling and collisional properties of a Rb-Cs mixture. *Phys. Rev. A* **71**, 061401.
47 Townsend, J.S. (1992) *A Modern Approach to Quantum Mechanics*, McGraw-Hill, New York, NY.
48 Silber, C., Günther, G., Marzok, C., Deh, B., W. Courteille, P., and Zimmermann,

C. (2005) Quantum-degenerate mixture of fermionic lithium and bosonic rubidium gases. *Phys. Rev. Lett.* **95**, 170408.

49 Marzok, C., Deh, B., Courteille, W.P., and Zimmermann, C. (2007) Ultracold thermalization of ^{7}Li and ^{87}Rb. *Phys. Rev. A* **76**, 052704.

50 Ketterle, W. and J. van Druten, N. (1996) Evaporative cooling of trapped atoms. *Adv. At. Mol. Opt. Phys.* **37**, 181.

51 Zobay, O. and Garraway, B.M. (2001) Two-dimensional atom trapping in field-induced adiabatic potentials. *Phys. Rev. Lett.* **86**, 1195.

52 Colombe, Y. (2004) *Condensat de Bose–Einstein, champs évanescents et piégeage bidimensionnel*, Ph.D. thesis, Université Paris 13.

53 Lesanovsky, I., Schumm, T., Hofferberth, S., Andersson, L.M., Krüger, P., and Schmiedmayer, J. (2006) Adiabatic radio-frequency potentials for the coherent manipulation of matter waves. *Phys. Rev. A* **73**, 033619.

54 Lesanovsky, I., Hofferberth, S., Schmiedmayer, J., and Schmelcher, P. (2006) Manipulation of ultracold atoms in dressed adiabatic radio-frequency potentials. *Phys. Rev. A* **74**, 033619.

55 Colombe, Y., Knyazchyan, E., Morizot, O., Mercier, B., Lorent, V., and Perrin, H. (2004) Ultracold atoms confined in RF-induced two-dimensional trapping potentials. *Europhys. Lett.* **67**, 593.

56 White, M., Gao, H., Pasienski, M., and DeMarco, B. (2006) Bose–Einstein condensates in RF-dressed adiabatic potentials. *Phys. Rev. A* **74**, 023616.

57 van Es, J.P.J., Whitlock, S., Fernholz, T., van Amerongen, H.A., and van Druten, J.N. (2008) Longitudinal character of atom-chip-based RF-dressed potentials. *Phys. Rev. A* **77**, 063623.

58 Hofferberth, S., Fischer, B., Schumm, T., Schmiedmayer, J., and Lesanovsky, I. (2007) Ultracold atoms in radio-frequency dressed potentials beyond the rotating-wave approximation. *Phys. Rev. A* **76**, 013401.

59 Loftus, T., Regal, C.A., Ticknor, C., Bohn, J.L., and Jin, D.S. (2002) Resonant control of elastic collisions in an optically trapped Fermi gas of atoms. *Phys. Rev. Lett.* **88**, 173201.

60 Jervis, D. (2007) *Fabrication of an atom chip*, Master's thesis, Department of Physics, University of Toronto.

61 Gati, R., Albiez, M., Foelling, J., Hemmerling, B., and Oberthaler, M.K. (2006) Realization of a single Josephson junction for Bose–Einstein condensates. *Appl. Phys. B* **82**, 207.

62 Estève, J., Gross, C., Weller, A., Giovanazzi, S., and Oberthaler, M.K. (2008) Squeezing and entanglement in a Bose–Einstein condensate. *Nature advanced online publication*.

63 DeMarco, B. and Jin, D.S. (1998) Exploring a quantum degenerate gas of fermionic atoms. *Phys. Rev. A* **58**, R4267.

64 Busch, T., Anglin, J.R., Cirac, J.I., and Zoller, P. (1998) Inhibition of spontaneous emission in Fermi gases. *Europhys. Lett.* **44**, 1.

65 Shuve, B. and Thywissen, J.H. (2010) Enhanced Pauli blocking of light scattering in a trapped Fermi gas. *J. Phys. B: At. Mol. Opt. Phys.* **43**, 015301.